AGU PUBLICATIONS

Geophysical Research Letters

RESEARCH LETTER
10.1002/2016GL069564

Key Points:
- P and S reflection and conversion responses from transmitted teleseisms
- Three components of teleseismic events are used rather than ambient noise
- Broader-frequency band of response helps to reveal finer-scale structure

Supporting Information:
- Supporting Information SI

Correspondence to:
W. Sun,
swj@mail.iggcas.ac.cn

Citation:
Sun, W., and B. L. N. Kennett (2016), Receiver structure from teleseisms: Autocorrelation and cross correlation, *Geophys. Res. Lett.*, *43*, 6234–6242, doi:10.1002/2016GL069564.

Received 11 MAY 2016
Accepted 8 JUN 2016
Accepted article online 13 JUN 2016
Published online 29 JUN 2016

Receiver structure from teleseisms: Autocorrelation and cross correlation

Weijia Sun[1] and B. L. N. Kennett[2]

[1]Key Laboratory of Earth and Planetary Physics, Institute of Geology and Geophysics, Chinese Academy of Sciences, Beijing, China, [2]Research School of Earth Sciences, Australian National University, Canberra, ACT, Australia

Abstract We present a way of characterizing the structure beneath a seismic station, by exploiting stacked correlograms of three-component records from teleseismic events. This seismic daylight imaging approach exploits the extraction of reflection and conversion information from teleseismic coda via tensor autocorrelation. The approach is illustrated for a number of Australian stations in a variety of tectonic environments using hundreds of teleseismic events, to extract *P* and *S* reflectivity and converted *Ps* and *Sp* information. The results show a very good agreement with prior knowledge across Australia. Compared with the classical receiver function, the broader-frequency band of 0.5–4.0 Hz provides additional information on finer-scale structure.

1. Introduction

In seismology, the receiver function method proposed by *Vinnik* [1977], *Langston* [1979], and *Vinnik et al.* [1983] has been extensively applied to detecting the discontinuities beneath seismic stations. The receiver function was initially designed to exploit the converted waves and reverberations behind the initial *P* onset for distant events. In this *Ps* receiver function the converted *SV* waves follow the first *P* arrival (Figure 1b). Subsequently, *Farra and Vinnik* [2000] extended the idea to the *Sp* receiver function, using *P* conversions from incident *S* that arrive ahead of the teleseismic *S* arrival (Figure 1c).

Ps receiver functions have played an important role in studies of the topography of the Moho and the mantle transitions near 410 km and 660 km depth. However, crustal reverberations have pronounced interferences with the *Ps* conversions from the depth range 100–250 km, which leads to difficulties in imaging the lithosphere-asthenosphere boundary with *Ps* receiver functions [*Kumar and Bostock*, 2006; *Ford et al.*, 2010]. In contrast, the *Sp* receiver function can overcome this shortcoming, since the converted *Sp* waves arrive earlier than *S*, while the crustal multiples occur later than the first *S* arrival. Nonetheless, the applications of *Sp* receiver functions are limited by the frequency content of teleseismic *S*, low signal-to-noise ratios [*Kumar and Bostock*, 2006], and interference with other phases, e.g., *SKS* and *SKSp*, for epicentral distance beyond 75° and *P* wave phases, e.g., *pPPP*, for events with focal depth larger than 300 km [*Ford et al.*, 2010].

Claerbout [1968] proposed an attractive method to construct acoustic reflections from transmitted waves via an autocorrelation procedure. His results were extended to elastic waves at nonvertical incidence by *Frasier* [1970]. Initially somewhat of a theoretical curiosity, the idea has subsequently given rise to two distinct strands of work.

Wapenaar et al. [2004] derived the relations between the reflection and transmission responses in 3-D heterogeneous media and expressed the reflection response in term of the cross correlation of the transmission response from two stations, a form of seismic interferometry (SI) [*Wapenaar et al.*, 2010]. With the help of numerical modeling, *Draganov et al.* [2006] succeeded in constructing the reflection response from upgoing transmitted waves generated by transient sources with distinct excitation or noise sources. Seismic interferometry exploiting cross correlations between stations has been used to image the Moho using teleseismic events recorded by a dense receiver line with station interval of 0.9–1.2 km [*Abe et al.*, 2007] and lithospheric structures using average station interval of 2.6 km [*Ruigrok et al.*, 2010]. For this approach with linear arrays the teleseismic events need to lie close to the great circle through the stations [*Ruigrok et al.*, 2010]. This restriction has been avoided by *Draganov et al.* [2013] in small-scale SI work with a receiver interval of 6.25 m and the exploitation of ambient noise to extract reflections from ambient noise. For these SI-based methods, at least two stations are needed per wavelength, conditions which are not commonly met for earthquake studies.

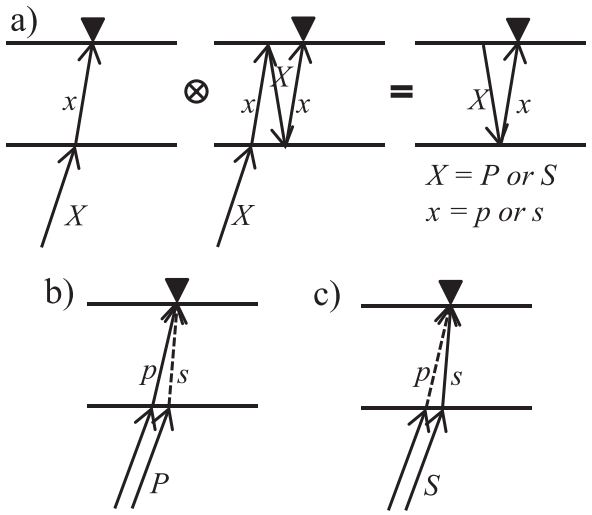

Figure 1. Sketch illustrations of raypaths for constructing reflection responses from transmitted waves recorded at a single station: (a) for both *P* and *S* waves in comparison with the (b) *Ps* receiver function and the (c) *Sp* receiver function. The reflections extracted by the principle shown in Figure 1a are equivalent to zero-offset seismograms with a surface source and receiver at the same location. The separation of surface reflections is only used for convenience in display.

An alternative approach based on the *Claerbout* [1968] concept is to work with a single station. *Kumar and Bostock* [2006] developed an autocorrelation and cross-spectra method to retrieve reflections from transmitted waves using a single component or vector components recorded at an individual station in 1-D homogeneous elastic media. Their method relies on isolating first-order scattering and was successfully applied to the station HYB in India using teleseismic arrivals. *Gorbatov et al.* [2013] constructed stacked station autocorrelograms for Australian stations, using the full continuous record on the vertical component. In this way they could exploit any earthquake contributions and also use the ambient noise to construct the Green's function for a coincident source and receiver. The initial application by *Gorbatov et al.* [2013] was to crustal *P* wave reflectivity across the continent. This approach has since been used by *Kennett et al.* [2015] to extract improved Moho structure in southeastern Australia exploiting records from more than 750 stations, including stations with only single component recording for which receiver functions could not be used. *Kennett* [2015] probed the *P* reflectivity in the lithosphere beneath Australia, and into the asthenosphere, exploiting broadband stations.

Here we adopt a somewhat different approach and concentrate on the contribution from significant teleseismic events to illuminate the structure beneath the station. This can be termed "seismic daylight imaging" by analogy with optics, as used in oceanography [*Buckingham et al.*, 1992] and by *Schuster et al.* [2004] to describe Claerbout's idea. Because the azimuth of the source is known, it is possible to effectively exploit both *P* and *S* waves to extract both *P* and *S* reflectivity from component autocorrelations. Further component cross correlation yields results equivalent to *Ps* and *Sp* receiver functions, with a broader frequency range than in the standard approach. We illustrate the method by application to a set of permanent stations across Australia, in a variety of geological environments.

2. Principle

Claerbout's original concept and its extensions apply autocorrelation to convert transmitted waves from sources below discontinuities into an equivalent reflection record; the results depend on the presence of the free surface. Thus, teleseismic event arrivals, as planar waves propagating near vertically from distant sources to surface receivers, provide an ideal illumination of receiver-side discontinuities in the upper mantle. Once the first *P* arrivals encounter the free surface, the surface reflected waves propagate downward and are then subsequently reflected back again to the surface by discontinuities in the interior of the Earth. The raypaths are indicated in Figure 1a. Similar effects occur for all subsequent *P* waves impinging on the free surface. The surface-related multiples are generally hidden in the *P* coda and are difficult to directly identify but are extracted by their consistent autocorrelation properties.

At a three-component station the ground motion contains *P* waves dominantly on the vertical component and, after rotation of the horizontal components, *SV* waves on the radial component and *SH* waves on the transverse component. For stratified isotropic media, the *P-SV* components are decoupled from the *SH* component. Here we focus on retrieving reflections for *P* and *SV* waves.

The principle is most simply represented in the frequency domain. We write $Z(\omega)$ and $R(\omega)$ for the vertical and radial components of the seismic wavefield at the surface from teleseisms at angular frequency ω. Then the *PP* reflections $U_{PP}(\omega)$ can be extracted as [*Gorbatov et al.*, 2013]

$$U_{PP}(\omega) = Z^*(\omega)Z(\omega), \tag{1}$$

where the asterisk indicates complex conjugation, since the transform of an autocorrelation is the power spectrum. When both the radial and vertical components are used we have the tensor relation

$$\begin{pmatrix} U_{PP} & U_{Ps} \\ U_{Sp} & U_{SS} \end{pmatrix} = \begin{pmatrix} Z^* & 0 \\ 0 & R^* \end{pmatrix} \begin{pmatrix} Z & R \\ Z & R \end{pmatrix}. \tag{2}$$

Here the subscript *SS* denotes the *SV* reflection response, while *Ps* and *Sp* denote the wave conversions from discontinuities, and as we shall see are similar to the *Ps* and *Sp* receiver function.

The arrivals from teleseismic events do not propagate purely vertically beneath the station. For *P* phases the slowness values ranges from ~4.4 to 8.8 s/deg with decreasing epicentral distance; for *S* the practical range is ~8.0 to 12 s/deg, since this avoids the larger slowness range in which there is strong coupling to *P* waves in the crust (equivalent to shear-coupled PL arrivals).

To reconstruct the reflection response at vertical incidence, we need to apply a moveout correction to the autocorrelograms for each individual teleseismic event before stacking. The procedure is somewhat similar to that used for receiver functions. In the $\tau - p$ domain, the moveout correction can be expressed as

$$\tau_0 \approx \tau/(1 - \frac{1}{2}v_0^2 p^2), \tag{3}$$

where τ_0 is the vertical reflection time for slowness p, τ is the real reflection time, and v_0 is the average velocity above an interface. This result is derived in the supporting information Text S1. It should be noted that the moveout corrections in the slowness domain are negative, although the corresponding corrections in the $t-x$ domain are positive. We can minimize the corrections needed by initially phasing to a reference slowness p_r in the teleseismic range before stack and then finally correcting the stack trace to vertical incidence.

In frequency domain, *Ps* receiver functions are defined as a deconvolution via spectral division as

$$\mathrm{RF}_{Ps}(\omega) = \frac{R(\omega)}{Z(\omega)}, \tag{4}$$

and the *Sp* receiver functions as

$$\mathrm{RF}_{Sp}(\omega) = \frac{Z(\omega)}{R(\omega)}. \tag{5}$$

Although the functional form is similar, different time windows are employed to construct the receiver functions. To enhance stability, the equations (4) and (5) are commonly recast as

$$\mathrm{RF}_{Ps}(\omega) = \frac{Z^*(\omega)R(\omega)}{\max[|Z(\omega)|^2, c \cdot \max(|Z(\omega)|^2)]}, \tag{6}$$

and

$$\mathrm{RF}_{Sp}(\omega) = \frac{R^*(\omega)Z(\omega)}{\max[|R(\omega)|^2, c \cdot \max(|R(\omega)|^2)]}, \tag{7}$$

with the division implemented by, e.g., a water-level procedure [*Helmberg and Wiggins*, 1971]. The terms $U_{Ps} = Z^*(\omega)R(\omega)$ and $U_{Sp} = R^*(\omega)Z(\omega)$ in equation (2) preserve the phase of the receiver functions. If a water-lever filter with value $c = 1$ is used in calculating the receiver function, equations (6) and (7) would be equivalent to the constructed responses by cross correlation of vector components. Therefore, the cross components can be considered as alternative implementations of the classical receiver functions [*Galetti and Curtis*, 2012]. In

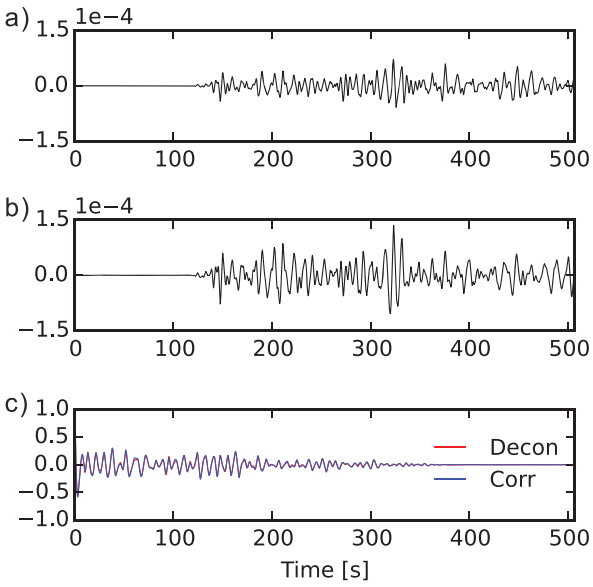

Figure 2. The (a) *R* component and (b) *Z* component of *P* and the *P* coda for an event recorded at station BBOO station. (c) Comparison of the U_{Ps} response with cross correlation (blue line) and the *Ps* receiver function with deconvolution (red line). The M_w8.6 earthquake occurred off the west coast of Sumatra at 08:38:37 11 April 2012.

Figure 2 we show the *Ps* receiver function and the constructed response U_{Ps}, using the same time windows, for a large teleseismic event off-Sumatra recorded at the BBOO station in southern Australia. There is a good match between the two different approaches for the timing of arrivals, but as expected the amplitudes are different.

The application of autocorrelation and cross correlation techniques extracts time delays for different phases arriving at a station. In Figure 1a, we see that autocorrelation leads to a *P* or *SV* reflection seismogram from a surface source with a surface receiver at the same location. In Figures 1b and 1c, cross correlation of vector components extracts the contributions from converted phases (*Ps* or *Sp*) recognized by their travel time differences from the first *P* or *SV* arrivals.

3. Data

We select teleseismic events during the period from 1 January 2010 to 31 December 2015 recorded at permanent stations across Australia for the epicentral distance range 30°–90° for *P* and *S* reflectivity, *Ps*, and *Sp* receiver functions. The preprocessing data procedures are the same as for regular receiver functions. Waveforms with signal-to-noise ratios (SNR) below 2 are discarded. The noise is selected from the time window of 60 to 30 s before the theoretical *P* arrivals predicted by the *ak*135 model, while the signal is taken over the time window between −5 s and 5 s relative to the predicted *P* arrivals. The SNR is defined as a ratio of the root-mean-square of signal and noise taken from the vertical components. After selection, the number of suitable teleseismic events found for further processing range from 93 events at station YNG to 197 events at station WRAB.

Prior to autocorrelation and cross correlation, all waveforms on both the vertical (*Z*) and radial (*R*) components are bandpass filtered with corners at 0.1–5 Hz, a broader- and higher-frequency range than commonly used in receiver function studies, which gives the possibility of finer resolution of structure. In Figure 3, we display time-frequency analysis for each component to show the frequency characteristics of the raw teleseismic signals at the stations BBOO and FORT, using the same large off-Sumatran event. As expected the higher frequencies are reduced for *S*, because of greater attenuation along the propagation path, though are still significant.

After autocorrelation and cross correlation an extra bandpass filter of 0.5–4 Hz for *P* and 0.5–3 Hz for *S* is employed. To suppress the large amplitude in the autocorrelations at zero time, a one-sided Hanning window function is used for the first 5 s.

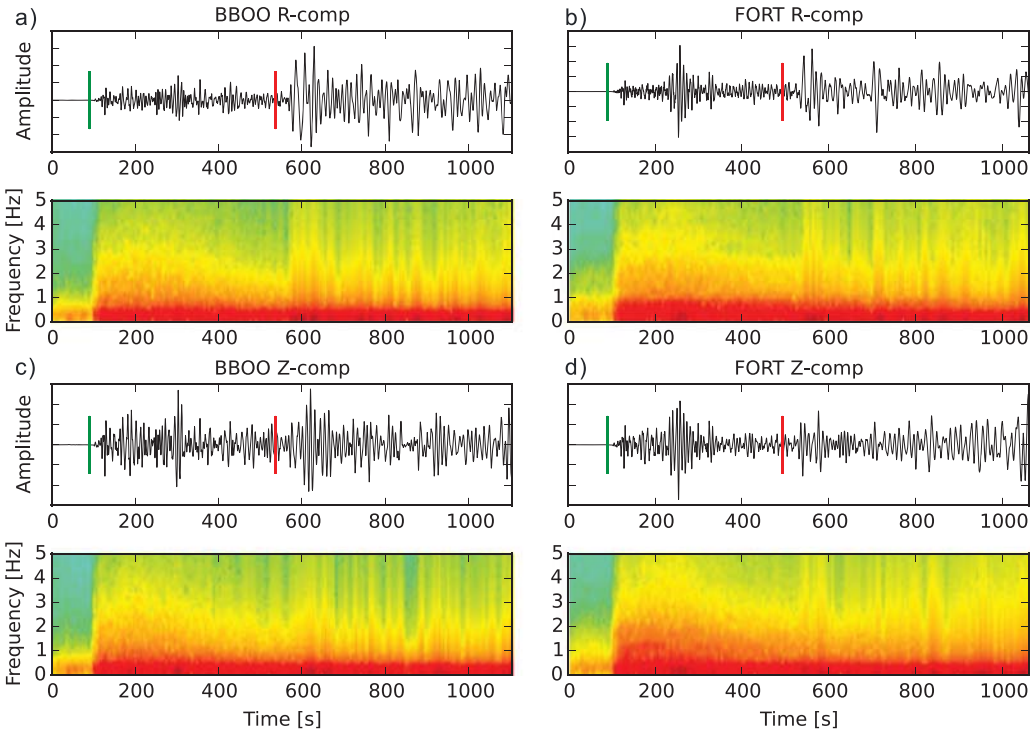

Figure 3. Time-frequency analysis of seismogram recorded at the stations (a, c) BBOO and (b, d) FORT. The top panel shows radial (*R*) components (Figures 3a, and 3b) and the bottom panel shows the vertical (*Z*) components (Figures 3c and 3d). The green line indicates the *P* arrival, and the red line the *S* arrival predicted by the *ak*135 model [*Kennett et al.*, 1995]. The same event is used as shown in Figure 2.

4. Results

In Figure 4 we show the suite of Australian permanent stations for which results are presented in Figure 5. The positions of the stations in Figure 4 are superimposed on the Moho depth distribution compiled from refraction, reflection, and receiver function studies [*Salmon et al.*, 2013]. We select a group of stations with similar locations to those used by *Ford et al.* [2010] to investigate the lithosphere-asthenosphere boundary beneath Australia, which were also employed by *Gorbatov et al.* [2013] for crustal *P* reflectivity from stacked autocorrelograms of continuous data from the vertical component and *Kennett* [2015] for lithospheric *P* reflectivity. These stations are located in the Precambrian Cratons in western and central Australia and in the Phanerozoic orogens along the eastern margin of the Australian continent.

The results of the seismic daylight imaging are displayed in Figure 5, where for each station we show the results of autocorrelation of the vertical and radial components and the cross correlations. The traces are constructed by stacking the contributions from the teleseisms with satisfactory signal-to-noise for *P*, *SV* reflectivity, and cross correlograms. The moveout corrections (3) are applied to each autocorrelogram trace before stacking. Here the moveout corrections are carried out using the *ak135* model [*Kennett et al.*, 1995], which represents a good continental average. After the application of the moveout corrections with time shift and slight waveform stretch, the stacked traces are equivalent to those slowness $p = 0$ (vertical incident below stations).

We use a flexible window, for *P*, of 100 s before the *P* arrival and 50 s before the *S* arrival predicted by the *ak*135 model [*Kennett et al.*, 1995], and for *S* a window 650 s long starting 100 s before the predicted *S* arrival. In this way we can examine the *P* and *SV* reflectivity in the lithosphere beneath the stations and compare with the results extracted from converted phases.

The Moho from Figure 4 is converted to time using an average *P* crustal wave speed of 6.0 km/s as in *Gorbatov et al.* [2013] and *SV* wave speed of 3.3 km/s. The expected Moho times are indicated on the autocorrelation

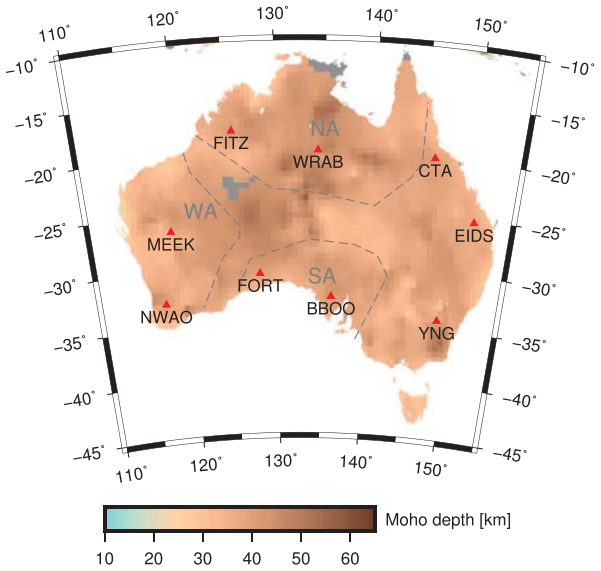

Figure 4. The Moho depth across the Australian continent from *Salmon et al.* [2013]. The red triangles denote the locations of the permanent stations. The simplified cratonic boundaries are given by the gray lines: NA, Northern Australia; SA, Southern Australia; and WA, Western Australia.

and cross-correlation traces in Figure 1 by a vertical red line. For comparison of the performance of the four responses from equation (2), we align the Moho reflections by taking the *PP* response as the reference.

In Figure 5 we show the stacked autocorrelation and cross correlation results for a number of stations across Australia in a variety of geological environments. The top two panels for each station in Figure 5 show the *PP* and *SS* reflectivity estimated from the stacked autocorrelograms for the vertical and radial components. Only the shallow part of the *SS* reflectivity can be expected to stack effectively, and so we mask the *SS* response after 35 s two-way time.

In the bottom two panels of Figure 5, we compare the converted responses of U_{Ps} and U_{Sp} obtained by cross correlation with the *Ps* and *Sp* receiver functions constructed by deconvolution in frequency domain. For all stations, the U_{Ps} results agree well with the *Ps* receiver function though there are differences in the detail of the amplitude, which are likely to be associated with changes in the spectrum produced by the stabilized numerical implementation of deconvolution. We note that the amplitudes of the receiver function around 5 s are much weaker than the corresponding correlation responses. Similar variations are found between the U_{Sp} response and the *Sp* receiver function.

As pointed out by *Kennett et al.* [2015] it is relatively unusual for the Moho to be marked by strong reflectivity, generally it marks a change in the style of reflection response at the base of the crust. In the *PP* and *SS* reflections, the *PmP* and *SmS* reflections can be tracked through changes in frequency characteristics, rather than a single prominent reflector as a marker of the Moho [*Kennett*, 2015]. This behavior is illustrated in Text S3 of the supporting information with model simulation.

With the aid of the moveout corrections for *P* waves we can expect to achieve a suitable rendering of the *P* wave reflectivity through the full thickness of the lithosphere. However, for *S* waves, the teleseismic regime is less suitable (as discussed in Text S2 in the supporting information). Beyond 40 s two-way time, it is likely that even the moveout corrections are not sufficient to achieve coherent stacking. Nevertheless, the shallow results for *S* should still be useful.

A particularly clear reflector is seen for the *PP* reflection for the station NWAO in the Archean Yilgarn craton near 13 s in Figure 5g, which corresponds to the expected reflection from the Moho. In contrast the *SS* reflection does not show a prominent reflector, but rather a distinct change in the character of the reflection series. Both the *Ps* and *Sp* responses also tie well with the Moho depth.

The station FORT lies on the Nullabor limestones with a complex near-surface structure that leads to strong reverberations, which makes it difficult to work with the *Ps* receiver function [*Ford et al.*, 2010] (Figure 5e).

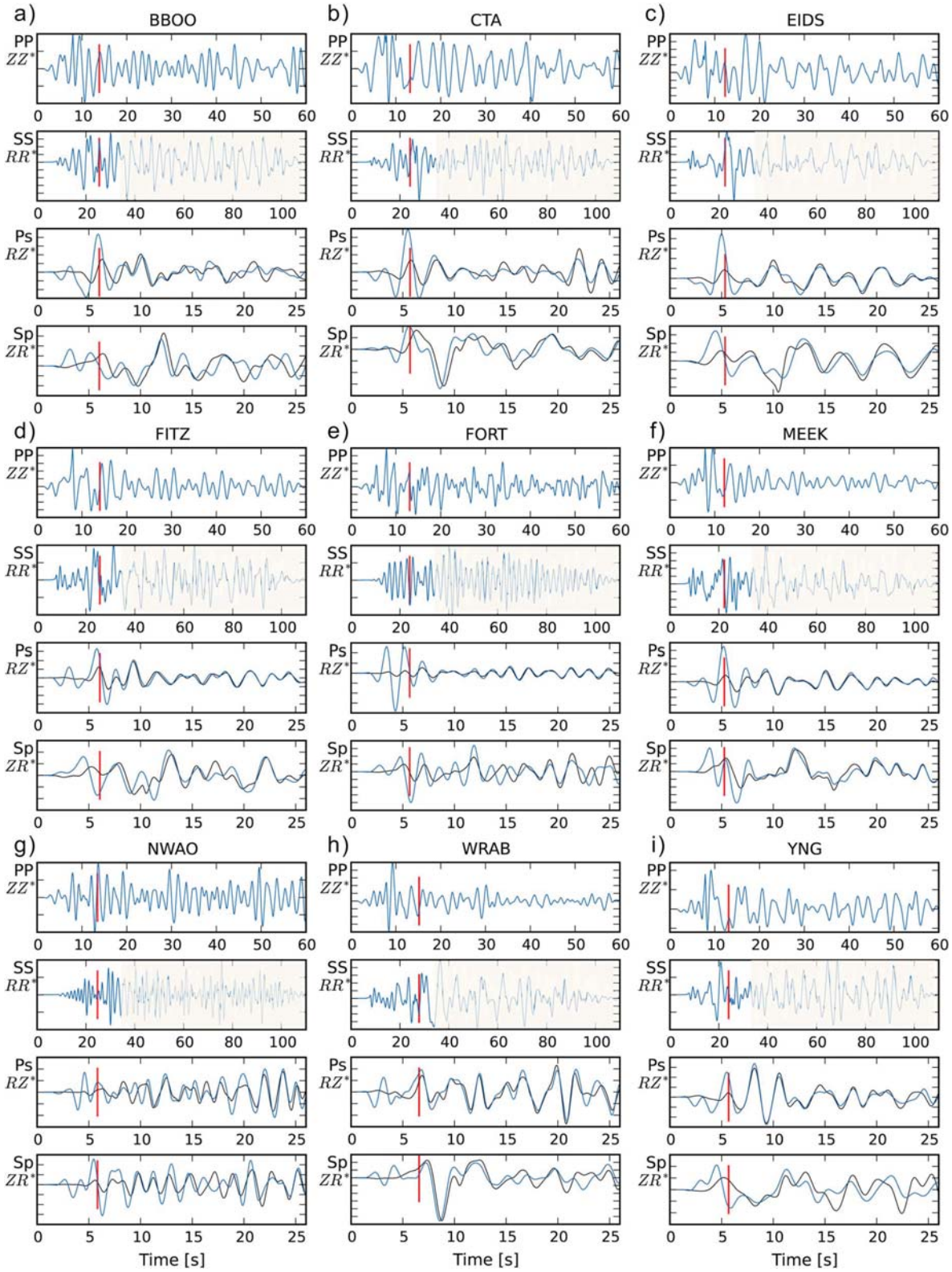

Figure 5. Results calculated using tensor correlation (2) for stations shown in Figure 4: (a) BBOO, (b) CTA, (c) EIDS, (d) FITZ, (e) FORT, (f) MEEK, (g) NWAO, (h) WRAB, and (i) YNG. Each subfigure has four subpanels denoting *P* and *SV* autocorrelograms, and *Ps* and *Sp* cross correlograms from top to bottom. The vertical red lines denote the Moho time converted from depth with approximated average *P* velocity of 6.0 km/s and *S* velocity of 3.3 km/s. The black lines in the lower two panels for each station show the *Ps* and *Sp* receiver function for comparison.

Nevertheless, a distinct change in the frequency pattern of crustal reflectivity can be recognized in the *PP* reflections at 13 s, which agrees directly with recent seismic reflection profiling that passes within 100 m of the permanent seismic station. The variations in frequency characteristics provide a strong indicator of the extent of crustal reflectivity for other stations across the continent.

The *PP* reflection traces in Figure 5 sample down to about 230 km. The lithospheric reflectivity from the stacked autocorrelograms of teleseismic arrivals agree well with the results presented by *Kennett* [2015] using stacked autocorrelograms from continuous records and, therefore, also including a contribution from ambient noise. Although there is significant return of seismic energy from beneath the Moho, there is no single prominent reflector that would automatically be identified as either the lithosphere-asthenosphere boundary or the midlithosphere discontinuity. There is, however, often a slight change in *PP* or *SS* reflection response at the time corresponding to the feature identified by *Ford et al.* [2010] from *Sp* receiver functions.

5. Discussion and Conclusions

We exploit the minor arrivals in teleseismic wave trains to extract reflection and conversion information from the waves transmitted to individual seismic stations. The reflection response in this seismic daylight imaging exploits the correlograms of multicomponent seismic data. The *P* and *SV* reflectivity can be found from the autocorrelograms of the vertical and radial components, whereas the cross correlograms provide information comparable to *Ps* and *Sp* receiver functions with appropriate selection of trace segments. The approach is very flexible and can readily be applied to both sparse and dense configurations of seismic stations.

Because the approach works with data from just a single station it can be distinguished from the concept of seismic interferometry defined as the principle of generating seismic observations at different receiver locations by *Wapenaar et al.* [2010]. Further, since specific teleseismic events are employed it is possible to orient the horizontal components of the seismogram and so work directly with the *SV* and *SH* components of the arrivals. *Gorbatov et al.* [2013] demonstrated good results for *P* waves from stacked autocorrelograms of the vertical components of continuous seismic records. However, the indiscriminate mixture of *S* polarizations in the ambient noise component makes analysis of the equivalent *S* results much more challenging.

The selection of very distant seismic events with small slownesses means that the arrivals are close to vertical. For a study of the Tibetan Plateau *Ruigrok and Wapenaar* [2012] employed global *P* phases with slowness smaller than 4.4 s/deg, e.g., *PKP* and *PKIKP*, to extract *P* reflectivity. For small slownesses the coherence of different reflectivity estimates is expected to be high (see Text S2 of the supporting information); however, frequently it is difficult to collect enough global phases because of limited seismicity on the other side of the Earth as *Ruigrok and Wapenaar* [2012] explicitly commented for their study exploiting the High-Climb array in the Himalaya. This is, unfortunately, also the situation for the Australian continent, with few events of suitable magnitude at large epicentral distances.

We further verify the abilities of teleseisms to build reflections by synthesizing autocorrelograms from incident plane wave with different slownesses for both *P* and *S* as shown in the supporting information. Figure S1 demonstrates that teleseismic events with slowness between 4.4 and 8.8 s/deg for *P* are suitable to retrieve *P* reflections from the Moho. Since *S* has larger slowness than *P* for teleseismic events, it is favorable to use these events with the moveout correction (3) to extract *S* reflectivity for distant events. In this paper, we apply the moveout correction for both *P* and *S* waves to improve the later reflections.

The seismic daylight responses are retrieved from *P* coda and *S* coda by correlation and moveout correction, and are then stacked to improve the signal-to-noise ratio. As pointed out by *Ruigrok and Wapenaar* [2012], the implementation of autocorrelation can create both physical and spurious reflections. The stacking procedure helps to reduce the effects of nonphysical cross terms, since the teleseismic arrivals have a range of incident slownesses. Spurious reflections can also be effectively suppressed by selecting the time windows containing a single dominant phase and its reverberations between free surface and discontinuities.

Further, although the *PP*-reflection results include full free-surface effects, the reflection coefficients are small for these steeply traveling *P* waves. Thus, multiple trains generated from the free surface rapidly diminish in amplitude. This is contrast to the situation for *Ps* receiver functions where the *s* energy gives rise to both reflections and conversions with strong multiple trains for complex near-surface structure. Therefore, multiple reflections generated at the surface are not detrimental to the retrieved reflectivity from transmission responses, except for the very near surface.

Compared with regular receiver function techniques, the autocorrelograms of *PP* and *SS* reflections and the cross correlograms for *Ps* and *Sp* allow access to the full available frequency band for body waves (0.25–4 Hz) above the microseismic peak (~ 0.125 Hz). In contrast, receiver functions employ waveforms with narrower-frequency band of 0.03–1 Hz for *Ps* and 0.03–0.5 Hz for *Sp* [e.g., *Ford et al.*, 2010]. In Figure 5, we use the same frequency band for both receiver functions and correlograms for a fair comparison. The *Sp* receiver functions with different frequency bands are compared with the autocorrelograms in the supporting information. With a broader-frequency band, finer sampling can be achieved for the crust and the upper mantle.

The full range of *P* and *S* information from a single style of analysis aids the interpretation of finer-scale structures beneath a station, e.g., through recognition of changes in frequency content. Although we have here concentrated on *P* and *SV* waves, there is a fully anisotropic analog of the identity established by *Frasier* [1970]. This means that the tensor correlation procedure in (2) can be extended to all three components, with the extraction of *SH* reflectivity and the equivalent of transverse component receiver functions for *Ps*. Such additional information can be expected to throw further light of fine-scale anisotropic effects, as in the work of *Wirth and Long* [2014].

Acknowledgments
This work has been carried out at the Research School of Earth Sciences, The Australian National University. The research was supported in large part by the State Key Laboratory of Lithospheric Evolution, Institute of Geology and Geophysics, Chinese Academy of Sciences and the National Natural Science Foundation of China (grant 41474105), with additional support from the AuScope AuSREM project. The waveform data for the Australian permanent stations were retrieved from the IRIS Data Management Center (http://www.iris.edu/).

References

Abe, S., E. Kurashimo, H. Sato, N. Hirata, T. Iwasaki, and T. Kawanaka (2007), Interferometric seismic imaging of crustal structure using scattered teleseismic waves, *Geophys. Res. Lett.*, *34*, L19305, doi:10.1029/2007GL030633.

Buckingham, M. J., B. V. Berknout, and S. A. Glegg (1992), Imaging the ocean with ambient noise, *Nature*, *356*(6367), 327–329.

Claerbout, J. F. (1968), Synthesis of a layered medium from its acoustic transmission response, *Geophysics*, *33*(2), 264–269.

Draganov, D., K. Wapenaar, and J. Thorbecke (2006), Seismic interferometry: Reconstructing the Earth's reflection response, *Geophysics*, *71*(4), SI61–SI70.

Draganov, D., X. Campman, J. Thorbecke, A. Verdel, and K. Wapenaar (2013), Seismic exploration-scale velocities and structure from ambient seismic noise (>1 Hz), *J. Geophys. Res. Solid Earth*, *118*, 4345–4360, doi:10.1002/jgrb.50339.

Farra, V., and L. Vinnik (2000), Upper mantle stratification by *P* and *S* receiver functions, *Geophys. J. Int.*, *141*(3), 699–712.

Ford, H. A., K. M. Fischer, D. L. Abt, C. A. Rychert, and L. T. Elkins-Tanton (2010), The lithosphere-asthenosphere boundary and cratonic lithospheric layering beneath Australia from *Sp* wave imaging, *Earth Planet. Sci. Lett.*, *300*(3), 299–310.

Frasier, C. W. (1970), Discrete time solution of plane *P-SV* waves in a plane layered medium, *Geophysics*, *35*(2), 197–219.

Galetti, E., and A. Curtis (2012), Generalised receiver functions and seismic interferometry, *Tectonophysics*, *532–535*, 1–26.

Gorbatov, A., E. Saygin, and B. L. N. Kennett (2013), Crustal properties from seismic station autocorrelograms, *Geophys. J. Int.*, *192*(2), 861–870.

Helmberg, D., and R. A. Wiggins (1971), Upper mantle structure of midwestern United States, *J. Geophys. Res.*, *76*(14), 3229–3245.

Kennett, B. L. N., E. R. Engdahl, and R. Buland (1995), Constraints on seismic velocities in the Earth from traveltimes, *Geophys. J. Int.*, *122*(1), 108–124.

Kennett, B. L. N., E. Saygin, and M. Salmon (2015), Stacking autocorrelograms to map Moho depth with high spatial resolution in southeastern Australia, *Geophys. Res. Lett.*, *42*, 7490–7497, doi:10.1002/2015GL065345.

Kennett, B. L. N. (2015), Lithosphere-asthenosphere *P*-wave reflectivity across Australia, *Earth Planet. Sci. Lett.*, *431*, 225–235.

Kumar, M. R., and M. G. Bostock (2006), Transmission to reflection transformation of teleseismic wavefields, *J. Geophys. Res.*, *111*, B08306, doi:10.1029/2005JB004104.

Langston, C. (1979), Structure under Mount Rainier, Washington, inferred from tele-seismic body waves, *J. Geophys. Res*, *84*, 4749–4762.

Ruigrok, E., X. Campman, D. Draganov, and K. Wapenaar (2010), High-resolution lithospheric imaging with seismic interferometry, *Geophys. J. Int.*, *183*(1), 339–357.

Ruigrok, E., and K. Wapenaar (2012), Global-phase seismic interferometry unveils *P*-wave reflectivity below the Himalayas and Tibet, *Geophys. Res. Lett.*, *39*, L11303.

Salmon, M., B. L. N. Kennett, and E. Saygin (2013), Australian seismological reference model (AuSREM): Crustal component, *Geophys. J. Int.*, *192*(1), 190–206.

Schuster, G. T., J. Yu, J. Sheng, and J. Rickett (2004), Interferometric/daylight seismic imaging, *Geophys. J. Int.*, *157*(2), 838–852.

Vinnik, L. P. (1977), Detection of waves converted from *P* to *SV* in the mantle, *Phys. Earth Planet. Inter.*, *15*(1), 39–45.

Vinnik, L. P., R. A. Avetisjan, and N. G. Mikhailova (1983), Heterogeneities in the mantle transition zone from observations of *P*-to-*SV* converted waves, *Phys. Earth Planet. Inter.*, *33*(3), 149–163.

Wapenaar, K., J. Thorbecke, and D. Draganov (2004), Relations between reflection and transmission responses of three-dimensional inhomogeneous media, *Geophys. J. Int.*, *156*(2), 179–194.

Wapenaar, K., D. raganov, R. Snieder, X. Campman, and A. Verdel (2010), Tutorial on seismic interferometry: Part 1–Basic principles and applications, *Geophysics*, *75*(5), 75A195–75A209.

Wirth, E. A., and M. D. Long (2014), A contrast in anisotropy across mid-lithospheric discontinuities beneath the central United States—A relic of craton formation, *Geology*, *42*, 851–854.